Coherent quasielastic neutron scattering from NbD_x

H. Dosch and J. Peisl
Sektion Physik der Universität München, D-8000 München 22, Federal Republic of Germany

B. Dorner
Institut Laue-Langevin, Boîte Postale No. 156x, 38042 Genoble Cédex, France
(Received 27 June 1986)

The quasistatic local lattice distortions around individual interstitial deuterium defects in niobium have been investigated by means of coherent quasielastic neutron scattering. The important experimental issues of this study are discussed in detail. We compare the observed absolute scattering cross section with various model calculations in which many different defect locations and the associated Kanzaki forces are tested. The results show that the heretofore anticipated defect models are insufficient to describe the local defect environment. A new model which takes into account the occurrence of diffusion-induced nonequilibrium distortions is able to describe virtually all of our experimental findings. By this analysis we confirm on one hand that D in Nb is preferentially located at tetrahedral sites. We demonstrate on the other hand that a partial triangular site occupancy has to be taken into account, which is associated with a perturbed flight phase of the highly mobile defect. The evidence in our study of local nonequilibrium distortions sheds new light on the cubic symmetry of the force dipole moment and on other distortion-mediated defect properties.

I. INTRODUCTION

Information on the location of a point defect in the lattice and the induced static lattice distortions is essential for the understanding of many defect properties, such as its interaction with internal and external strain fields, its diffusion behavior, and its local vibration spectrum. Great efforts have been devoted in the last two decades to the study of the defect structure of interstitial hydrogen in transition metals[1] and a variety of puzzling results have been observed. In this introductory section we summarize this somewhat confusing situation which has sparked this neutron scattering study.[2]

The defect location of H,D in Nb,Ta has been investigated extensively by many different methods,[3–5] and, even though none of the experimental results provided totally unambiguous answers, there is an agreement that interstitial hydrogen is *preferentially* located at tetrahedral sites [Figs. 1(a) and 1(b)] and that octahedral site occupancy [Fig. 1(a)] can be ruled out. Steward[6] has pointed out that ambiguities in the defect location may not be due to deficiencies in the employed experimental methods but to inherent properties of the metal-hydrogen system under consideration. In this context it is quite instructive to discuss the preliminary results of a neutron structure analysis of NbD_x in the disordered α-α' phase.[7] Figure 2 shows the D-concentration dependence of the obtained R ("reliability") factor for the NbD_x structure with D assumed on tetrahedral, octahedral, and triangular sites [see Fig. 1(a)]. It is demonstrated that the octahedral sites are not occupied throughout the entire concentration range covered by the experiment; a unique distinction between a tetrahedral or a triangular site occupancy, however, seems impossible. A reanalysis by one of the authors revealed that one has to

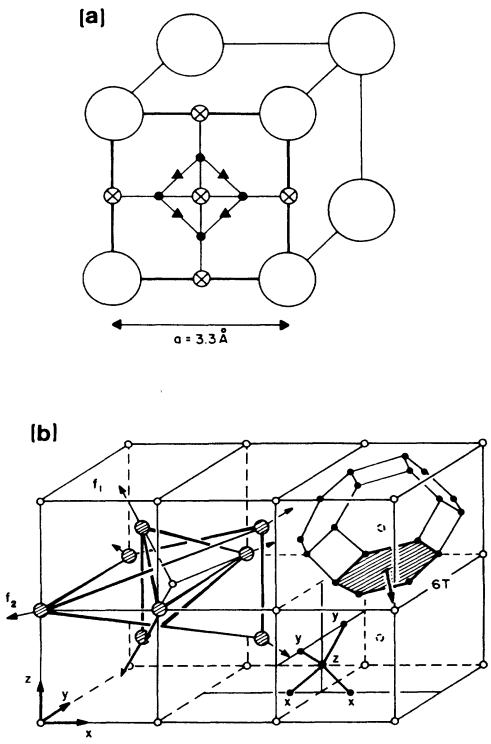

FIG. 1. (a) Locations of light interstitials in bcc metals: ●, tetrahedral site; ⊗, octahedral site; ▲, triangular site. (b) Left: Kanzaki forces on the nearest (f_1) and second-nearest- (f_2) neighbor atoms around one occupied tetrahedral site; right: tetrahedral 6T configuration and the location of the four nearest tetrahedral sites around one z-tetrahedral site.

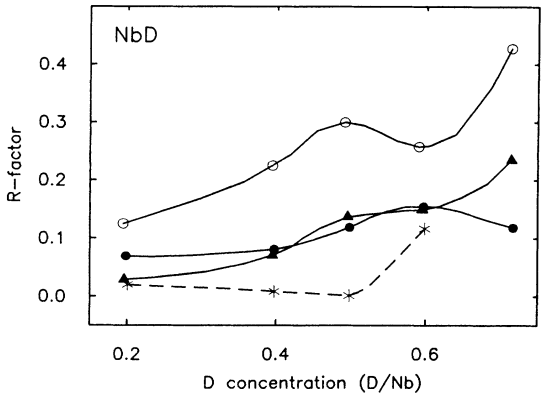

FIG. 2. Reliability factors ($R = \sum |I_{obs} - I_{cal}| / |I_{obs}|$) of a neutron structure analysis of disordered NbD_x for various D concentrations (Ref. 7): —●—, D on tetrahedral; —○—, octahedral; —▲—, triangular sites; —✱—, mixed tetrahedral-triangular site occupancy (1:1) (see text).

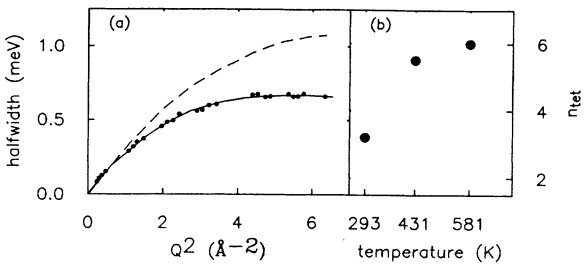

FIG. 3. Results from incoherent quasielastic neutron scattering (Ref. 12): (a) Incoherent linewidth versus Q^2: ●, experimental results; — — —, calculated from Chudley-Elliot model; ——, calculated from mobile-state model. (b) Number of tetrahedral sites (n_{tet}) in the mobile state versus temperature.

assume a mixed tetrahedral-triangular site occupation in the disordered α-α' phase in order to obtain the best agreement with the experimental results (dashed line in Fig. 2). The general increase of all R factors at higher D concentrations is apparently due to the occurrence of order fluctuations.[8] We will discuss below that low-symmetry sites, such as triangular sites, appear to be important to the understanding of the microscopic jumping behavior of the interstitial hydrogen.[9] (Note that two neighboring tetrahedral sites are separated by a saddle point which is a triangular site.)

Information about details of the hydrogen diffusion in bcc transition metals has been obtained in particular by *incoherent* quasielastic neutron scattering.[10,11] The Q dependence (Q=scattering vector) of the quasielastic linewidth provides distinct information about the macroscopic as well as the microscopic defect diffusion. A typical experimental result obtained for NbH_x is shown in Fig. 3(a).[12] The dashed line is calculated under the assumption that the defect performs jumps between neighboring tetrahedral sites in the framework of the Chudley-Elliot (CE) model.[13] The CE model assumes no correlations between individual jumps and neglects the so-called "flight phase" in the diffusion. Quite a few attempts have been made to extend the CE model,[14] but a first consistent description of the temperature and Q dependence of the quasielastic linewidth has been attained by Lottner *et al.*[12] through the introduction of a "two-state model" [solid line in Fig. 3(a)].

In the framework of this model the interstitial hydrogen is preferentially (see below) in a so-called "mobile state," where it performs fast, repeated jumps over several tetrahedral sites. This state decays with a certain rate into a second, "immobile state," where the defect stays in a tetrahedral site, and no diffusion jumps are allowed for some time. It turns out that, within this model, the probability of finding the mobile state occupied stays constant (0.67) in the measured temperature range, wheres the number of tetrahedral sites (n_{tet}) involved in the mobile state changes considerably with temperature [Fig. 3(b)]: At room temperature the mobile state consists of approximately three adjacent sites, and this number appears to saturate quickly at the value 6. This seems to indicate that the mobile state extends rapidly with temperature to the so-called "6T configuration" [Fig. 1(b)]. It is interesting to note that the 6T configuration (or 6T ring) has been suggested by a number of authors for bcc metal hydrides.

A rapid diffusion on a 6T ring was mentioned by Buchholz, Voelkl, and Alefeld[15] as a possible explanation of the absence of a Snoek relaxation in the systems NbH_x and TaH_x. Later, Abell[16] proposed a hydrogen-induced Jahn-Teller relaxation of the lattice which should stabilize a rapid 6T diffusion. Within a semiempirical, quantum-mechanical approach, Sugimoto and Fukai[17] discussed the dissolved proton and deuteron delocalized on a 6T ring.

The possible key to the understanding of the existence of mobile (delocalized) states should be found in the properties of the defect-induced lattice distortions. It is subsequently not too surprising that the static displacement field itself turned out to exhibit unusual features, too.

Measurements of the Snoek relaxation[15] and later of the Huang diffuse scattering of x rays[18] and neutrons[19] showed that the long-ranged part of the displacement field has cubic symmetry rather than the expected tetrahedral symmetry of the defect site. In the framework of the Kanzaki force formalism (see Sec. II) this discrepancy could only be settled by assuming that the Kanzaki forces around the occupied tetrahedral site are extended to the second-nearest neighbor [Fig. 1(b)] and that the strengths f_1 and f_2 of these forces fulfill the condition

$$f_1/f_2 = 4.35 \ . \tag{1}$$

We refer to this model in the following as the "tet_2 model" (for details see Sec. IV).

The lattice distortions in the close vicinity of the defect are less accessible to experimental methods, thus experimental evidence for this distortion field has been found so far only by two (x-ray) scattering studies. Dosch and Peisl[20] investigated the diffuse x-ray scattering at high-momentum transfers far away from Bragg points ("*Zwischenreflex* scattering") in the system $NbD_{0.04}$ and compared the results with numerical calculations. By this

analysis the observed diffuse scattering could be referred to the local distortions around defects which are mainly located at tetrahedral sites. Metzger *et al.*[21] report measurements of the defect-induced static Debye-Waller factor (e^{-2L}) in the disordered system NbH_x. Since L is given by[22]

$$L(\mathbf{Q})=c_D(1-c_D)\left\langle \sum_m [1-\cos(\mathbf{Q}\cdot\mathbf{u}_m^p)] \right\rangle_p \tag{2}$$

(where c_D is the defect concentration, $\mathbf{u}_m^p$ the local lattice distortion of the host lattice atom m in the presence of a defect at p, and $\langle\ \rangle_p$ the average over all occupied sites p), the experimental results (Fig. 4) allow conclusions on the local distortions around the defect. The dashed line is calculated using the tet_2 model and is distinctly different from the observations. This could be regarded as a first evidence that the proposed tet_2 model is not yet correct, however, since static displacements are in general accompanied by slight changes in the vibrational amplitudes, the observed mismatch between theory and experiment can also be referred to this effect (solid line in Fig. 4). We come to this point (and in particular to the dotted line in Fig. 4) in further detail in Sec. V.

II. COHERENT DIFFUSE SCATTERING DUE TO POINT DEFECTS

This field has been discussed by many authors.[22–24] For an introduction to this subject we refer the reader to the article by Dederichs.[24]

The diffuse scattering cross section for randomly distributed point defects has the form

$$S_{\mathrm{dif}}(\mathbf{Q})=c_D b^2\left\langle \left| b_D/b e^{i\mathbf{Q}\cdot\mathbf{R}_p-M_D} + \sum_n (e^{i\mathbf{Q}\cdot\mathbf{u}_n^p}-1)e^{i\mathbf{Q}\cdot\mathbf{R}_n} \right|^2 \right\rangle_p , \tag{3}$$

where b,b_D are the coherent scattering lengths of the host lattice atom and the defect, respectively ($b(\mathrm{Nb})=0.71$ fm, $b_D(\mathrm{D})=0.67$ fm).[25] The quantity $M_D=\frac{1}{2}\mathbf{Q}^2\langle v_{\mathrm{loc}}^2\rangle$ accounts for the mean-square vibrational amplitude $\langle v_{\mathrm{loc}}^2\rangle$ of the defect.

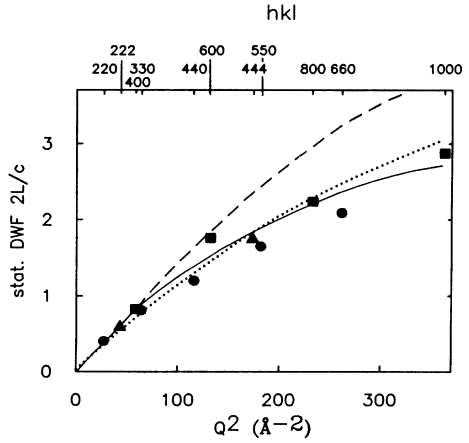

FIG. 4. Static Debye-Waller factor ($2L/c$) in NbH_x (Ref. 21): ■, ●, ▲, experimental results in the (100), (110), (111) direction; — — —, calculated from standard tet_2 model; ——, calculated from standard tet_2 model and introducing changed local vibrations; · · · ·, mobile-state model (see Sec. V).

The lattice sum $\sum_n$ over the entire long-ranged static displacement field $\mathbf{u}_n^p$ can be reduced to a local sum $\sum_n^{\mathrm{NN}}$ over the close defect vicinity by splitting up the linear term $i\mathbf{Q}\mathbf{u}_n^p$ in the above phase factor $\exp(i\mathbf{Q}\mathbf{u}_n^p)$. Then one gets[26]

$$\sum_n (\cdots)=i\mathbf{Q}\tilde{\mathbf{u}}^p(\mathbf{Q})+\sum_n^{\mathrm{NN}}(e^{i\mathbf{Q}\cdot\mathbf{u}_n^p}-1-i\mathbf{Q}\mathbf{u}_n^p)e^{i\mathbf{Q}\cdot\mathbf{R}_n} . \tag{4}$$

The Fourier transform $\tilde{\mathbf{u}}^p(\mathbf{Q})=\sum_n \mathbf{u}_n^p\exp(i\mathbf{Q}\cdot\mathbf{R}_n)$ becomes particularly simple in the Kanzaki force formalism,[27,28] where elastic forces $\mathbf{f}_n$ are introduced which act only on the host lattice atoms of the nearest-neighbor shells around the defect. One can show that $\tilde{\mathbf{u}}^p(\mathbf{Q})$ is related to the Fourier transform $\tilde{\mathbf{f}}^p(\mathbf{Q})$ of the force field by the dynamical matrix $\underline{\tilde{D}}(\mathbf{q})$ ($\mathbf{q}=\mathbf{Q}-\mathbf{G}_{hkl}$; $\mathbf{G}_{hkl}$ reciprocal-lattice vector):

$$\tilde{u}_i^p(\mathbf{Q})=\sum_j [\tilde{D}_{ij}(\mathbf{q})]^{-1}\tilde{f}_j^p(\mathbf{Q}) \tag{5}$$

(i,j are the Cartesian coordinates).

The inverse transformation yields the displacement field itself:

$$u_{mi}^p=\sum_{n,j} G_{ij}^{m-n}f_{nj}^p . \tag{6}$$

Quantitative values for the lattice Greens functions $\underline{G}^{m-n}$ and the dynamical matrix $\underline{\tilde{D}}(\mathbf{q})$ are deduced from measured phonon dispersion relations of the host lattice.[29]

In the defect models presented in this study we will parametrize the local lattice distortions by *radial* Kanzaki forces $\mathbf{f}_n^{(s)}$ applied at the atoms $\mathbf{R}_n^{(s)}$ of the shell s. This can be expressed as follows:

$$\mathbf{f}_n^{(s)}=f_s\frac{\mathbf{R}_n^{(s)}-\mathbf{R}_p}{|\mathbf{R}_n^{(s)}-\mathbf{R}_p|} , \tag{7}$$

with the values f_s ("force strength") being bound by the experimentally determined force dipole moment

$$P_{ij}^{(p)}=\sum_{s,n}(\mathbf{R}_n^{(s)}-\mathbf{R}_p)_i f_{nj}^{(s)} \tag{8}$$

(see also Sec. IV).

For arbitrary scattering vectors $\mathbf{Q}$ the scattering cross section of Eq. (3) has to be calculated numerically.[30] From the input parameters $\mathbf{R}_p$ and $f_s(s=1,2,3,\ldots)$ the Kanazaki field $\mathbf{f}_n$ follows [Eq. (7)]. The subsequent calculation of $\mathbf{u}_n^p,\tilde{\mathbf{u}}^p(\mathbf{Q})$, according to Eqs. (5) and (6) and from this finally $S_{\mathrm{dif}}(\mathbf{Q})$ from Eqs. (3) and (4), is relatively straightforward.

III. EXPERIMENTAL DETAILS

A. Sample preparation

Two Nb single crystals have been spark cut into cylinders of 50 mm length and 10 mm diameter with the

cylinder axis parallel to the ⟨110⟩ direction. Both crystals have been degassed at 2300 °C under UHV conditions for 60 h in order to purify them from the light impurities N, O, and C and to anneal dislocations. One crystal has then been doped with deuterium in a HV furnace, where the sample was heated to 600 °C and exposed to D_2 atmosphere. While the momentary deuterium uptake was controlled by reading the gas pressure decrement, we determined the final D concentration by the weight increase of the sample and found $c_D=0.017$. This result was also confirmed by measurements of the lattice parameter change (x-ray diffraction at the flat cylinder faces).

By means of neutron diffraction (performed at D13c, Grenoble) we found the bulk mosaic spread of the two crystals to be $\eta(\mathrm{Nb})=0.15°$ and $\eta(\mathrm{NbD}_x)=0.20°$. For a special test experiment (see below) another pure Nb crystal with a much larger mosaic spread of $\eta=0.73°$ has been prepared in the same way.

B. Quasielastic neutron scattering

The fundamental experimental problem in precise absolute measurements of the elastic-diffuse scattering far away from reciprocal-lattice vectors is the extremely weak signal compared to the diffuse scattering background. X-ray scattering in this regime of the scattering vector is dominated by strong Compton incoherent and temperature diffuse scattering. Dosch and Peisl[20] showed in the case of $NbD_{0.04}$ that the signal-to-background ratio there is only 0.1 or less. They could overcome this intensity problem by the use of high-power x-ray sources (60 kW rotating anode) and of position-sensitive detectors.

In the corresponding neutron scattering experiment the incoherent scattering and the inelastic scattering from phonon excitations contribute to the background intensity; however, the strong phonon scattering can be rejected experimentally by analyzing the energy of the scattered neutrons. Thus, by performing the experiment on a three-axis spectrometer run in a (quasi-) elastic mode the only dominant source for the scattering background is the *elastic* incoherent scattering, its cross section being

$$S_{\mathrm{inc}}(\mathbf{Q})=\frac{\sigma_{\mathrm{inc}}}{4\pi}\exp[-2M(\mathbf{Q})](1+K^D_{\mathrm{inc}}) , \tag{9a}$$

$$K^D_{\mathrm{inc}}=c_D\frac{\sigma^D_{\mathrm{inc}}}{\sigma_{\mathrm{inc}}}\exp[-2M_D(\mathbf{Q})+2M(\mathbf{Q})] , \tag{9b}$$

where $\sigma_{\mathrm{inc}},\sigma^D_{\mathrm{inc}}$ are the incoherent scattering power of the host lattice atom and the defects, respectively.

In the case of Nb, σ_{inc} is small (0.27 b) (Ref. 25) and can be determined by a reference measurement with a pure Nb crystal. Note that the correction term K^D_{inc} does not appear in the refernce measurement ($c_D=0$) and, thus, has to be calculated in order to get the correct values of S_{inc}. Since the ratio $\sigma^D_{\mathrm{inc}}/\sigma_{\mathrm{inc}}$ (7.44 in the case of NbD_x) (Ref. 25) and the defect concentration are known very accurately, K^D_{inc} can be accounted for without uncertainties.

The signal-to-(incoherent) background ratio should then be (neglecting Debye-Waller factors)

$$S/N(\mathbf{Q})=\frac{4\pi S_{\mathrm{dif}}(\mathbf{Q})}{\sigma_{\mathrm{inc}}}=1-1.5 \tag{10}$$

for $c_D=0.02$ and $S_{\mathrm{dif}}(\mathbf{Q})=20-40$ mb (estimated from standard defects models, see below).

The experiments have been performed on the three-axis machine IN2 (Institut Laue-Langevin, Grenoble) with an incident wave vector $\mathbf{k}_I=5.4$ Å^{-1} [provided by a Cu(220) double monochromator] and a beam collimation of 120-60-60-60 min. The neutrons which were scattered from the sample within a quasielastic energy window were analyzed by a (004) pyrolytic graphite. The high incident neutron energy ($E_I=60$ meV) and the coarse beam collimation assured a relatively large resolution in **Q** space (adjusted to the weak and delocalized scattering). The energy resolution at energy transfer $\Delta E=0$ has been determined to be $\Delta\omega_0=3.8$ meV. Due to the rapid motion of the interstitial deuterium (see Sec. I) the elastic-diffuse scattering is broadened in energy (quasielastic scattering). Measurements of the incoherent quasielastic linewidth give values of $E_{\mathrm{inc}}\leq 1$ meV [see also Fig. 3(a)] for high **Q** values; thus, the large energy window $\Delta\omega_0$ of the spectrometer assured a reliable integration of the quasielastically broadened signal.

C. Experimental results

We discuss in what follows the experimental results obtained along the following two linear scans in reciprocal space (see also insets of Fig. 5):

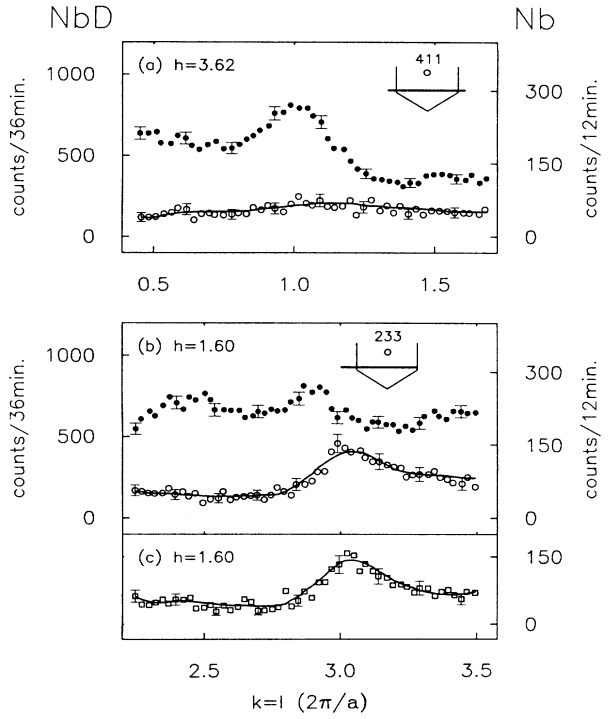

FIG. 5. Coherent quasielastic neutron scattering: (a),(b) Raw data obtained along scan 1 ($h=3.62$) and scan 2 ($h=1.60$) for $NbD_{0.017}$ (●) and Nb with $\eta=0.15°$ (○). (c) Raw data obtained along scan 2 for Nb with $\eta=0.73°$ (□). The solid lines are results of a cubic spline fit to the Nb data points. Note the different scales for the NbD_x and the Nb data.

$$\begin{aligned} &\text{scan 1 in BZ(411):}\quad \mathbf{Q}_n=(3.62,0.45,0.45)+n\cdot\Delta\mathbf{Q} \\ &\text{scan 2 in BZ(233):}\quad \mathbf{Q}_n=(1.60,2.25,2.25)+n\cdot\Delta\mathbf{Q} \\ &\qquad\qquad\qquad\qquad \text{with } \Delta\mathbf{Q}=0.025(0,1,1) \end{aligned} \tag{11}$$

(in units of $2\pi/a$), where BZ denotes Brillouin zone.

They have been chosen in order to provide high **Q** values in low-symmetry directions of different Brillouin zones far away from reciprocal-lattice vectors. These conditions are essential for obtaining maximum information on the local defect structure. [Note that, due to the phase $i\mathbf{Q}\cdot\mathbf{R}_p$ in Eq. (3) the diffuse scattering from interstitial defects does not exhibit the symmetry of the host lattice.] High-**Q** measurements are necessary for weakly distorting defects, because only waves scattered at high-**Q** values undergo a noticeable phase shift $i\mathbf{Q}\cdot\mathbf{u}_m^p$. Figures 5(a) and 5(b) show the raw data as obtained along scan 1 and scan 2. Note that the intensity scale for the $NbD_{0.017}$ and the Nb measurements has been adjusted to the corresponding data collection times (36 min/data point for $NbD_{0.017}$; 12 min/data point for Nb). We want to point out three factors.

(i) The observed counting rates are extremely low, as expected (approximately 15 counts/min in the case of $NbD_{0.017}$); therefore, the general neutron background in the experimental hall required careful consideration. By a proper shielding of the entire experimental setup an isotropic "zero level" of 3 counts/10 min could be achieved.

(ii) The observed feature in the reference measurement along scan 2 could be identified as an inelastic scattering contamination due to a nonzero transmission of the instrumental energy window for the transverse-acoustic phonon scattering at $\mathbf{q}=(0.4,0,0)2\pi/a$. As a coherent scattering process the inelastic phonon scattering is in general sensitive to the perfection of the crystal; however, its dependence on the mosaic spread should become negligible at greater distances from the Bragg points (as discussed here). This common argument has been confirmed experimentally by showing that the diffuse background along scan 2 measured from two Nb single crystals with distinctly different mosaic spreads $\eta=0.15°$ [background curve in Fig. 5(b)] and $\eta=0.73°$ [Fig. 5(c)] is virtually the same. Since the mosaic spread of the $NbD_{0.017}$ single crystal and the actual Nb reference crystal differed only by $\Delta\eta=0.05°$, the experimental elimination of the inelastic scattering in the difference spectrum can be considered as reliable.

(iii) In order to account for the larger statistical error of the background measurement, the background curves have been smoothed by a cubic spline function [solid lines in Figs. 5(a), 5(b), and 5(c)].

The coherent quasielastic diffuse scattering is found by subtracting the intensity of the reference crystal from the observed diffuse scattering. Because of the small defect concentration under discussion, the correction term K_{inc}^D for the incoherent scattering is only a minor effect ($K_{\text{inc}}^D\approx 0.12$). The conversion of the data into an absolute scale (barn) could be achieved with high accuracy by using the scattering intensity of some host lattice phonons (which have a well-known structure factor). This is discussed in detail in the Appendix.

IV. DISCUSSION

Detailed information on the local defect structure is obtained from the observed absolute intensity distribution by comparing it with numerical model calculations based on Eqs. (3)—(7). Three parameters enter into the models: (i) the defect location $\mathbf{R}_p$, (ii) the Kanzaki forces around the defect, and (iii) its local vibration $\langle v_{\text{loc}}^2\rangle$.

It turns out that the defect site $\mathbf{R}_p$ and, subsequently, the symmetry of the local distortions determine the main structural features of the diffuse intensity distribution, whereas details in the Kanzaki forces are reflected by the details in the absolute values of the scattering pattern. Since $\langle v_{\text{loc}}^2\rangle$ merely changes the coherent scattering length of the defect without affecting any phase shifts, only marginal effects are expected from a variation of this

TABLE I. Model parameters for the tetrahedral, octahedral, and triangular defect sites.

Site	Tetrahedral			Octahedral	Triangular
$\mathbf{R}_p(a/2)$	(1.5,1,0)			(1,1,0)	(0.75,0.75,0)
Model / Parameter	tet_1	tet_2	tet_3	oct_2	tri_2
Forces (eV/Å)	$f_1=1.0$	$f_1=1.0$ $f_2=0.23$	$f_1=1.2$ $f_2=0.20$ $f_3=-0.04$	$f_1=1.0$ $f_2=0.72$	$f_1=1.0$ $f_2=0.50$
P_{ij} (eV)	$\begin{bmatrix}1.47&0&0\\0&2.95&0\\0&0&2.95\end{bmatrix}$		$\begin{bmatrix}3.4&0&0\\0&3.4&0\\0&0&3.4\end{bmatrix}$		$\begin{bmatrix}2.5&0&0\\0&1.5&0\\0&0&1.5\end{bmatrix}$
χ^2 for $\langle v_{\text{loc}}^2\rangle$:					
0.010 Å^2		0.5181			
0.015 Å^2	0.8808	0.6142	1.2738	2.0202	0.6920
0.020 Å^2		0.7578			
χ^2 for the "tet-tri" model: 0.5687					

parameter. This hierarchy in the three parameters allows an independent determination of the defect location and its local lattice deformation.

A. Standard defect models

In the framework of these models the dissolved deuterium is localized at one interstitial site. The lattice atoms around the interstice are fully relaxed and describable by radial forces applied at the nearby host lattice atoms. The force strengths are bound by the experimentally established force dipole moment[15,18,19,31] [Eq. (8)]

$$P_{ij}(\mathrm{NbD}_x)=\begin{bmatrix}3.4 & 0 & 0\\ 0 & 3.4 & 0\\ 0 & 0 & 3.4\end{bmatrix}\ \mathrm{eV} \qquad (12)$$

which has cubic symmetry.

We discuss the tetrahedral, octahedral, and triangular defect sites (Fig. 1) which have been reported in the literature in the context of light impurities in bcc metals. The mean-square displacement $\langle v_{\mathrm{loc}}^2 \rangle$ has been set, according to Lottner and Schober,[32] to 0.015 Å^2, while the Kanzaki forces (f_1,f_2) are extended to the second-neighbor shell (models named tet_2, oct_2, and tri_2 in Table I). Note that the force field of the tet_2 model fulfills the condition of Eq. (1). The force dipole moment P_{ij} associated with the low-symmetry triangular sites, however, cannot be rendered cubic by only two independent Kanzaki forces; thus, this defect model would contradict the experimental evidence. (The special choice of this triangular Kanzaki force field assures that at least the off-diagonal elements of P_{ij} vanish; see also P_{ij} in Table I.) The diffuse scattering arising from these three models has been calculated numerically and compared with the experimental results [Figs. 6(a) and 6(b)].

From inspection of Figs. 6(a) and 6(b) we can conclude that none of the presented models is able to achieve a satisfactory agreement with the absolute experimental results; however, the best fit within these models is provided by the tetrahedral site which essentially reproduces all the *qualitative* features of the scattering pattern and gives also, according to the observed χ^2 values[33] (Table I), the best *quantitative* fit ($\chi^2=0.6142$). This confirms that deuterium in niobium is preferentially located at tetrahedral sites, while an eventual octahedral site occupancy can clearly be ruled out ($\chi^2=2.0202$). We note that the triangular model also exhibits a fit to the experimental values ($\chi^2=0.6920$) comparable to the tetrahedral model, a fact which again reveals the ambiguity previously suggested in the defect location (as discussed in Sec. I). By assuming a mixed tetrahedral-triangular site occupancy, the fit to the experimental data can indeed be improved [the dashed-dotted line in Figs. 6(a) and 6(b) is obtained by assuming a partial triangular occupancy of 50% and gives a fit quality of $\chi^2=0.5682$]; however, since this model (called "tet-tri" in the following) still cannot settle the striking discrepancies between theory and experiment, the additional free parameter (partial triangular occupancy) is irrelevant here.

The most important conclusion from this first analysis of the data is that in particular the Kanzaki force model

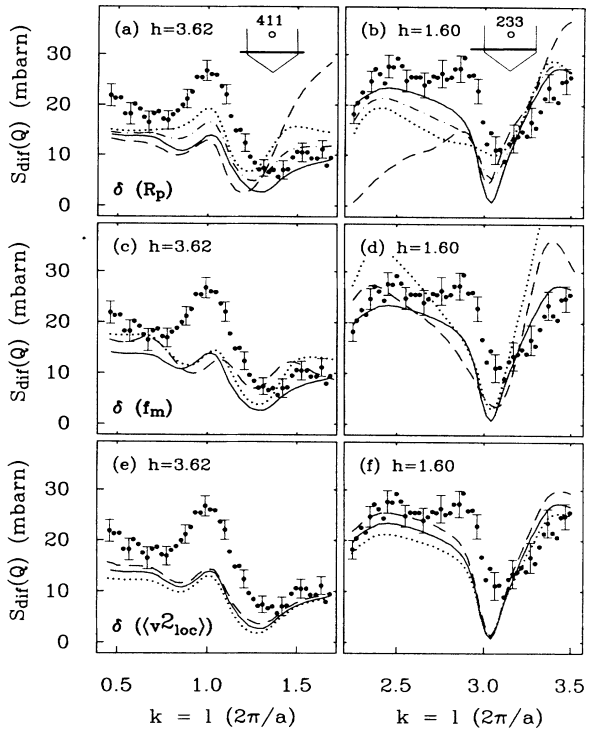

FIG. 6. Final experimental results (●) compared with standard defect models (Table I): (a),(b) ——, model tet_2; — — —, model oct_2; · · · ·, model tri_2; —·—, model tet-tri. (c),(d) — — —, model tet_1; ——, model tet_2; · · · ·, model tet_3. (e),(f) Model tet_2 with $\langle v_{\mathrm{loc}}^2 \rangle$=: — — —, 0.010 Å^2; ——, 0.015 Å^2; · · · ·, 0.020 Å^2.

deduced from Huang diffuse scattering (tet_2) cannot describe the local distortions around the defect. Thus the origin of the cubic long-ranged displacement field requires also a different explanation.

In order to settle the discrepancies between the measured and calculated scattering cross section we apply the following further analysis: We assume tetrahedral site occupancy and study the influence of the Kanzaki forces and the local vibrational amplitude of the deuterium on the coherent diffuse scattering cross section. Table I shows three different distortion models associated with the tetrahedral site with radial forces on the first-neighbor shell only (tet_1), on the first and second Nb neighbors (tet_2, same model as discussed before), and with extended forces up to the third-nearest neighbor (tet_3). The forces of model tet_2 and tet_3 reproduce the correct cubic dipole moment, whereas model tet_1 creates long-ranged displacements of tetrahedral symmetry. The calculated diffuse scattering from these models is tested with the measured scattering distribution in Figs. 6(c) and 6(d). The effect of a variation of $\langle v_{\mathrm{loc}}^2 \rangle$ between 0.010 and 0.020 Å^2 on the coherent scattering is shown in Figs. 6(e) and 6(f) for the defect model tet_2.

Inspection of Figs. 6(c) and 6(d) indicates that the cubic defect model tet_2 provides a better fit than the noncubic tet_1 model (see also the χ^2 values in Table I). However, a

further extension of the Kanzaki forces up to the third Nb neighborhood (tet_3) cannot settle the remaining intensity mismatches. From Figs. 6(e) and 6(f) and the corresponding χ^2 values in Table I, one may conclude that the mean-square amplitude of the defect appears a little smaller than 0.015 Å^2.

In summary we have ascertained that each of the models presented so far fails in a very distinct way to describe the observed data satisfactorily. The only possible conclusion is that the basic concept of the standard models (defect being self-trapped at one well-defined interstitial site, while the lattice is allowed for a full relaxation) is inadequate to describe the local distortions around deuterium in niobium.

B. Mobile-state model

The previous models did not in particular account for the mobility of the defects and assumed the defect fixed (immobile) at one interstitial site. It may appear to the reader as if this implicit assumption were not justified at all and that a correct description of the measured scattering cross section has to include the diffusion of the defect in some way. However, this general argument disregards the proper time scale involved in the measuring process under consideration. To put this important aspect into a correct perspective, we consider the intermediate scattering function of the defect alone which is

$$f_{pp'}(\mathbf{Q},t)=\langle \exp\{-i\mathbf{Q}\cdot[\mathbf{R}_p(t)-\mathbf{R}_{p'}(0)]\}\rangle \tag{13a}$$

and measures the correlation between the defect site $\mathbf{R}_{p'}(0)$ occupied at $t=0$ and the site $\mathbf{R}_p(t)$ occupied at a later time t. The energy distribution of the associated quasielastic scattering cross section is then

$$S_D(\mathbf{Q},\omega)=\int dt \exp(i\omega t)\sum_{p,p'} f_{pp'}(\mathbf{Q},t) \tag{13b}$$

and includes, of course, all the details of the microscopic diffusion of the defect; however, by integrating over all quasielastic energies we find that

$$\begin{aligned} S_D(\mathbf{Q}) &\equiv \int\int \exp(i\omega t)\sum_{p,p'} f_{pp'}(\mathbf{Q},t)\,dt\,d\omega \\ &= \sum_{p,p'} f_{pp'}(\mathbf{Q},t=0)\ . \end{aligned} \tag{14}$$

Thus, $S_D(\mathbf{Q})$ and correspondingly $S_{\rm dif}(\mathbf{Q})$, the quantity which is considered in this study [Eq. (3)], measure a "snapshot" at $t=0$ of the defect configuration (which is random in our case) and thus are independent of any diffusion processes. In this sense the applied standard defect models are fully justified and account, without approximation, for the real situation.

However, there is indeed the subtle assumption in the previous models that the lattice relaxation time is sufficiently small compared to the rest time of the defect at one interstitial site which assures that the full lattice relaxation around the momentarily occupied site can be established. Since the lattice relaxation usually occurs at a time scale comparable to typical phonon frequencies in the lattice ($\sim 10^{12}$ sec^{-1}), this is in most cases a well justified assumption. In the case of the rapid motion of interstitial hydrogen, on the other hand, this requires a more careful consideration, because the jumping frequency ω_j of hydrogen (deuterium) in Nb,Ta at room temperature is also as high as[34] 10^{11}–10^{12} sec^{-1}.

The dynamics of the lattice deformations accompanying the rapid motion of the defect can be understood in terms of phonon absorption and emission by the defect, where, depending on the spatial extent of the static displacement field, this may or may not be dominated by short-wavelength phonons. One time scale involved in this process is associated with the "dephasing" $\Delta\omega_{\rm ph}$ of the superposition of the corresponding normal modes (dephasing time $t_{\rm ph}$):

$$\Delta\omega_{\rm ph} t_{\rm ph}=\pi\ , \tag{15}$$

where the bandwidth $\Delta\omega_{\rm ph}$ is related to the spatial extent of the static displacement field by

$$\Delta\omega_{\rm ph}=\omega(2\pi/\lambda_c)\ . \tag{16}$$

$\omega(q)$ is the phonon dispersion of the system and λ_c the characteristic length scale of the distortion cluster. For a completely localized phenomenon ($\lambda_c=a_0$ lattice constant) one then gets the common answer that the dephasing frequency is comparable to the Debye frequency of the lattice. If the local distortions are more extended, $\Delta\omega_{\rm ph}$ becomes accordingly smaller. One obvious uncertainty lies in the definition of the extension of the lattice distortions, because they have long-ranged character. Therefore, one conjecture is[35] to relate λ_c to the dynamics of the defect itself by setting

$$\lambda_c=(2\pi/\omega_j)v_s \tag{17}$$

(v_s = typical sound velocity of the lattice), which would give an estimate value of $\lambda_c\approx 100$ Å (for $v_s\sim 10^5$ cm/sec). By inserting λ_c into Eqs. (16) and (17) we find $t_{\rm ph}\sim 10^{-11}$ sec. One can get away from the uncertainties in defining a characteristic length somewhat by looking instead at the elastic energy $E_{\rm el}$ which is stored in the lattice distortion. Emin[36] has estimated the time $t_{\rm dis}$ ("dissipation time") which governs the dissipation of the stored energy $E_{\rm el}$. (His work was concerned with the lattice deformations around hopping electrons.) One then finds that the Debye frequency ω_D, the elastic energy $E_{\rm el}$, and the dissipation time $t_{\rm dis}$ can be related by

$$t_{\rm dis}=\frac{6}{\pi\omega_D/2}\left[\frac{2E_{\rm el}}{kT}\right]^{2/3}\ , \tag{18}$$

giving again typical values of $t_{\rm dis}\sim 5\times 10^{-12}$ sec for $E_{\rm el}=169$ meV (Ref. 37). This indicates that the "dissipation frequency" $t_{\rm dis}^{-1}$ of the lattice and the hopping frequency of the defect are comparable in our case. Therefore, the approximation made in the standard models, $(t_{\rm dis})^{-1}\gg\omega_j$, appears to be strongly violated. This means that the rapid diffusion of the deuterium occurs within a region of the crystal where the local equilibrium is not achieved. From this viewpoint the rather anomalous diffusion behavior (fast, repeated jumps between several tetrahedral sites) as discussed in Sec. I and, of course, the difficulties (in this study) in describing the coherent dif-

fuse scattering cross section by means of fully relaxed defects appear no longer surprising.

We suggest that the occurrence of the so-called "mobile" and "immobile" states in the microscopic jump mechanism (see Sec. II) are intimately related to the dynamics of the lattice relaxations. In particular, the repeated jumps in the mobile state should be referred to the action of nonequilibrium lattice distortions, whereas the immobile state should be describable by standard (fully relaxed) lattice distortions.

According to the room-temperature results obtained by Lottner *et al.*,[12] there are three adjacent tetrahedral sites involved in the mobile state [see Fig. 3(b)]. The associated nonequilibrium relaxations can be introduced in the following way. We assume that the defect-lattice interaction can be parametrized by radial Kanzaki forces applied at the four nearest Nb neighbor atoms only. The distortions of the mobile state can then be approximated by a linear superposition of the three individual force fields with the advantage that only one free parameter, the force strength f_1 enters into the calculations. It turns out that $f_1 = 1.0$ eV/Å is a reasonable value (as suggested by the defect-induced homogeneous lattice expansion[31]).

One tetrahedral site (say, the z-tetrahedral site in the following) has four nearest tetrahedral neighbors. Inspection of Fig. 1(b) shows that there are two different types of "three-tetrahedral-site configurations ($3T$ configurations), one of type x-z-x and y-z-y and four of type x-z-y; thus, together six possible configurations. Since this holds as well for the x and z sites, there are 18 nonequivalent $3T$ configurations. The incoherent scattering data did not indicate any preferential jumping path; therefore, in the subsequent calculation we have to average over all 18 configurations. Figure 7 shows one x-z-y $3T$ configuration and the distortions of the neighboring Nb atoms. Apparently three different displacements should be distinguished: The atoms (000) and (111) experience the strongest distortions (u_1) due to the superposition of three individual Kanzaki forces; the atoms ($\bar{1}11$) and (020) undergo an intermediate distortion (u_2) because of the action of two forces; and the atoms ($11\bar{1}$) and (002) are only affected by one force and should have the smallest distortion (u_3). Note that this distortion field exhibits a preferential lattice distortion in the ⟨111⟩ direction, a fact which will be discussed in more detail in Sec. V.

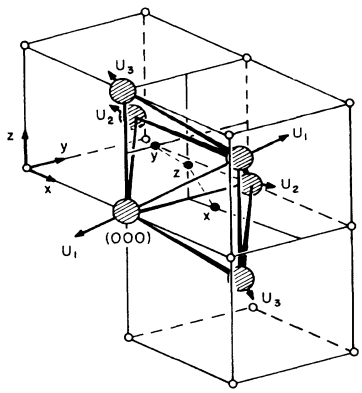

FIG. 7. Local structure of the x-z-y mobile state: (for u_1, u_2, and u_3, see text).

For the proper calculation of the coherent scattering cross section arising from the mobile states we have to remember that, due to the quasielastic integration, we "see" in our experiment the defect distribution and the lattice distortions at the time $t=0$. In this snapshot the hopping deuterium is located at one of the three tetrahedral sites surrounded by the nonequilibrium lattice deformations associated with the mobile state. Since the force strength f_1 is fixed, the corresponding scattering cross section $S_{\mathrm{mob},t}(\mathbf{Q})$ can be calculated without any free parameter. In each of the mobile states the deuterium may be found at three possible tetrahedral sites which has to be considered in the averaging procedure, giving $\langle S_{\mathrm{mob},t}(\mathbf{Q})\rangle_c$ [dashed line in Figs. 8(a) and 8(b)]. The angled brackets $\langle\ \rangle_c$ indicate the average over all occurring configurations.

There is another scattering contribution from the mobile state which has to be taken into account. In the discussion up to now we have implicitly assumed that the time period during which the hopping defect is located at a tetrahedral site ("rest time") is dominant compared to the time during which it is actually jumping ("flight phase"). This approximation, however, is most likely not fulfilled in our case. As the preferential location of the deuterium during the flight phase we assume the triangular saddle points between two adjacent tetrahedral sites. Thus, to allow for a finite flight phase within the mobile state we calculate the coherent scattering cross section, where the defect is located at one triangular site within the distorted region of the mobile state, and get $\langle S_{\mathrm{mob},tg}(\mathbf{Q})\rangle_c$ [dotted lines in Figs. 8(a) and 8(b)]. We have neglected any additional lattice relaxations arising from the flight phase; therefore, the only difference be-

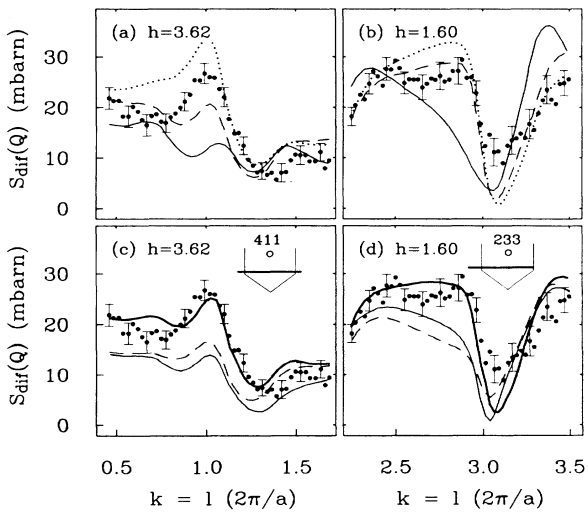

FIG. 8. Final experimental results (●) compared with the mobile-state model. (a),(b) ——, contribution of $\langle S_{\mathrm{im}}(\mathbf{Q})\rangle_p$; — — —, contribution of $\langle S_{\mathrm{mob},t}(\mathbf{Q})\rangle_c$; · · · ·, contribution of $\langle S_{\mathrm{mob},tg}(\mathbf{Q})\rangle_c$. (c),(d) Comparison of the optimal mobile-state model (boldface line) with the best fits within the standard model: ——, tet_2 model; — — —, tet-tri model.

tween the two cross sections $\langle S_{\text{mob},t}(\mathbf{Q})\rangle_c$ and $\langle S_{\text{mob},tg}(\mathbf{Q})\rangle_c$ is the location of the defect within the same lattice distortions. Inspection of Figs. 8(a) and 8(b) shows that the two scattering cross sections are significantly different in some parts of the reciprocal space; therefore, the distinction between the rest time and the flight time appears much simpler in the case of the *coherent* cross section than it is in the *incoherent* case.

The total coherent scattering cross section originating from the mobile state should accordingly be written as

$$S^{(\alpha)}_{\text{mob}}(\mathbf{Q})=\alpha\langle S_{\text{mob},t}(\mathbf{Q})\rangle_c+(1-\alpha)\langle S_{\text{mob},tg}(\mathbf{Q})\rangle_c\ , \tag{19}$$

with $0<\alpha<1$ as a free parameter.

The scattering cross section $S_{\text{im}}(\mathbf{Q})$ of the immobile state can still be calculated within the framework of the standard defect models. Since we parametrize the defect-lattice interaction by Kanzaki forces on the nearest-neighbor atoms, $S_{\text{im}}(\mathbf{Q})$ should be identical with the model tet_1 from above [solid lines in Figs. 6(c) and 6(d) and Figs. 8(a) and 8(b)].

The observed scattering is then governed by

$$S^{(\alpha\beta)}_{\text{tot}}(\mathbf{Q})=\beta S_{\text{im}}(\mathbf{Q})+(1-\beta)S^{(\alpha)}_{\text{mob}}(\mathbf{Q})\ , \tag{20}$$

where the free parameter $0<\beta<1$ describes the probability of finding an immobile state. The only two adjustable parameters α and β of our model can be determined by a least-squares fit of Eq. (20) to our experimental data. The best fit is shown as the bold lines in Figs. 8(c) and 8(d) and provides

$$\alpha=0.5\pm0.15,\quad \beta=0.2\pm0.10\ . \tag{21}$$

We note that our model is able to explain virtually all salient features of the observed coherent diffuse scattering, the quality of the fit being given by $\chi^2=0.1674$ which has to be compared with the best fits within the standard models. These are the tetrahedral model tet_2 [$\chi^2=0.6142$; solid lines in Figs. 8(c) and 8(d)] and the mixed tetrahedral-triangular occupancy model [$\chi^2=0.5682$; dashed lines in Figs. 8(c) and 8(d)]. Since all these models use two free parameters, the striking improvement of the new fit is considered to be strong evidence that the basic assumptions of the mobile state model are essentially correct.

The values obtained for the parameters have a straightforward significance. $(1-\beta)=0.8\pm0.1$ describes the probability for the occurrence of the mobile state. From the analysis of the incoherent quasielastic scattering[12] one finds the (temperature-independent) value 0.67. Note that the latter value is found from the energy distribution of the incoherent scattering, whereas our value stems from the energy-integrated coherent scattering; therefore, the virtual agreement of both results appears remarkable. The value $\alpha=0.5\pm0.15$ indicates that the flight time of the defect in the mobile state is severely perturbed by triangular minima and the local lattice distortions so that the concept of a free proton (deuteron) is not applicable. The subsequent partial triangular site occupancy seems to confirm the preliminary results of the above-mentioned neutron structure analysis of the high-temperature disordered phase (see Fig. 2).

It is important to realize that the mobile state model and the standard model tet-tri (mixed tetrahedral-triangular occupancy) both assume virtually the same triangular site occupancy. However, the crucial difference between the two models is the momentary lattice relaxations during the occupation of the triangular sites.

The final results in Eq. (21) enable us to calculate the properties of the mean dipole moment $\langle P_{ij}\rangle$ (associated with *one* tetrahedral site, but averaged over the mobile and immobile states). A simple calculation yields

$$\text{Tr}\langle P_{ij}\rangle=\beta\,\text{Tr}P^{(\text{im})}_{ij}+(1-\beta)\text{Tr}P^{(\text{mob})}_{ij}\approx 10\text{ eV}\ . \tag{22}$$

This agreement with the experimental value [Eq. (12)] should not be overemphasized, because it is essentially a consequence of the chosen force strength f_1. However, a nontrivial result is the symmetry of $\langle P_{ij}\rangle$: One finds from the symmetry of the mobile and immobile states that the deviation of $\langle P_{ij}\rangle$ from cubicity, defined as $\langle t\rangle\equiv\langle(P_{11}-P_{22})/\text{Tr}P_{ij}\rangle$, has the small value

$$\langle t\rangle=0.05\pm0.02 \tag{23}$$

and is thus very close to the experimentally observed cubic symmetry of the long-ranged part of the displacement field ($t=0$). Note that the applied Kanzaki forces fully preserve the tetrahedral symmetry of the defect site ($t^*=0.2$). The virtual disappearance of the noncubic parts of the (quasi-) static lattice displacements is on our model due to the fact that the host lattice atoms around the highly mobile defect cannot reach their new equilibrium positions. Thus, we conclude that the observed cubic symmetry of the force dipole tensor should not be referred to as the defect-lattice interaction (as parametrized by the cubic two-force field), but as the presence of not fully relaxed mobile states.

According to Eq. (23), very small noncubic components in the force dipole moment still remain and have to be addressed separately: They should in principle be detectable in the Huang diffuse scattering and in the Snoek relaxation, both experimental methods being sensitive to t^2. This means that the ratio of the observed effect ($\langle t\rangle=0.05$) and the expected effect ($t^*=0.2$ according to the symmetry of the defect site) is proportional to $(\langle t\rangle/t^*)^2$ and thus only 6%. Experiments performed so far provide only upper limits of $t\lesssim0.03$ (Ref. 15) and $t\lesssim0.02$ (Ref. 18). Within the experimental error both limits are not inconsistent with our value of $\langle t\rangle=0.05\pm0.02$. We want to note that the uncertainty in $\langle t\rangle$ has been calculated only from the error in the parameter β. However, the reader should keep in mind that the two-state model adopted in our analysis also buries some simplifications, e.g., neglecting the existence of preferential diffusion paths or discarding deviations of the Kanzaki forces from the applied one-force field which preserves the full tetrahedral symmetry of the defect site. These still unknown model parameters can slightly vary the present value of $\langle t\rangle$ and may be considered in future refinements of the present model. We also note at this point that our analysis is based on the experimental results from the incoherent quasielastic linewidth and their interpretation in terms of the two-state model. Therefore, our final defect model cannot be considered unique, but rather

as a simple heuristic model to account for a very complex physical situation.

C. Immediate consequences

The experimental evidence of nonequilibrium lattice distortions which has been discussed in this study sheds a new light on many properties of the dissolved hydrogen. One of them, the anomalous microscopic diffusion mechanism, has been discussed in detail in this paper. However, there are many other implications of these new results, some of which will be addressed in this section.

1. Hydrogen trapping

Some aspects of the mechanism of the trapping of hydrogen at impurities, like oxygen and nitrogen, and the possible trapping configurations should be reconsidered, in particular the semiempirical calculations[38] which assumed the standard (cubic) two-force model (tet_2). According to our results, the trapped hydrogen should be described as an immobile state and thus parametrized by noncubic forces. Since the trapping of hydrogen removes all the mobile states, changes in the symmetry of the hydrogen-associated force dipole moment, in particular, an increase of noncubic elements, can be expected as a new trapping effect.

2. Local modes

Local modes appear hard to include into the new picture of mobile states. However, one has to keep in mind that the time scale associated with the local modes is of the order of 10^{-13} sec, thus, two orders of magnitude faster than the rest time of the defect. Therefore, local modes can even be established during the rapid motion of the defect in the mobile state. Interestingly enough, the observed energy widths of these modes do exhibit unusually large values and do become smaller when the defect is trapped at N or O.[39] Possible sources of a large width of the local defect modes can be a distribution of local environments and/or a restricted lifetime of the modes due to a short rest time of the defect. Both mechanisms are clearly provided by the introduced nonequilibrium distortions. The narrowing of the energy widths in the trapped state is then a consequence of the reduced mobility of the defect.

3. Temperature dependence of lattice distortions

Temperature dependence of lattice distortions is expected because the nonequilibrium distortions are influenced by the diffusion of the defect. Unfortunately, measurements at low temperatures are strongly affected by hydrogen precipitations so that the effect of a decrease in the mobility of the defect appears hard to observe. In a preliminary study we have instead performed a 480-K measurement of the coherent diffuse scattering along scan 2 and have compared it to the room-temperature results (Fig. 9). The slight increase of the diffuse intensity maximum can be understood in the following way. From the above quantitative analysis we know that the major contribution to the observed diffuse intensity maximum stems from the flight phase of the defect in the mobile state [see dotted line in Figs. 8(a) and 8(b)]. Therefore, the intensity increase with temperature seems to indicate that the spatial extent of the mobile states has increased as suggested by the analysis of the incoherent scattering.[12]

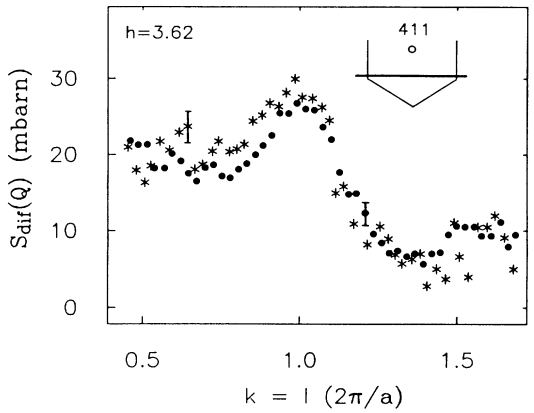

FIG. 9. Final experimental results of the coherent quasielastic neutron scattering obtained along scan 1 for two different temperatures: ●, 300K; ∗, 480 K.

4. Static Debye-Waller factor (SDWF)

The interpretation of the SDWF (Ref. 21) assumed that the local distortions correspond to *one* local defect environment as described by the tet_2 model. In this study we have shown that the case is much more complicated and that a variety of local distortions (due to the occurrence of mobile and immobile states) has to be taken into account. Therefore, while the principle analysis of the SDWF as presented by Metzger *et al.*[21] is correct, the quantitative conclusions certainly have to be modified in some way.

Consider again Fig. 7 which shows the local environment of a mobile state. As pointed out in Sec. III, three different distortions u_1, u_2, and u_3 occur, u_1 being the dominant displacement which affects the two atoms (000) and (111). It appears remarkable to us that a distortion along the ⟨111⟩ direction has also been found to be created by a (quasimolecular) Jahn-Teller relaxation in bcc metal hydrides.[16] Thus, one may speculate as to whether the u_1 distortion, in combination with the suggested Jahn-Teller effect, could be another stabilizing element for the mobile-state configurations.

In the framework of this work the SDWF has the form

$$2L(\mathbf{Q})=2\beta L_{\mathrm{im}}(\mathbf{Q})+2(1-\beta)L_{\mathrm{mob}}(\mathbf{Q}) , \tag{24}$$

where both individual contributions $2L_{\mathrm{im}}$ and $2L_{\mathrm{mob}}$ (associated with the immobile and mobile states) have to be calculated according to Eq. (2). The result of a numerical calculation based on the Eqs. (2), (21), and (24) is shown as the dotted line in Fig. 4 and provides certainly a satisfactory fit to the experimental data. From this analysis we find the three distortions of the mobile states to be $u_1=0.12$ Å, $u_2=0.05$ Å, and $u_3=0.02$ Å, and a distortion $u_1'=0.1$ Å of the four nearest Nb neighbors in the

immobile states. Therefore, the experimental evidence that the observed $2L$ values are lower than anticipated by the tet_2 model is, within the mobile-state model, due to the fact that the fast diffusion of the defect does not allow the full local lattice relaxation. Since the change in the local vibrations of the disturbed Nb atoms (as proposed by Metzger *et al.*[21] to obtain the solid line in Fig. 4) is sound, this additional parameter could be used to improve the fit. However, a statistical analysis of the problem makes this new variable irrelevant.

ACKNOWLEDGMENTS

One of us (H.D.) received financial support from the Institut Laue-Langevin (France) during the progress of this work, as well as from the School of Applied and Engineering Physics, Cornell University (USA) and the Alexander von Humboldt Foundation (West Germany) during the preparation of the manuscript. This work was supported by the Bundesministerium für Forschung und Technologie (West Germany). We are grateful to the Kristallabor der Technischen Universität München for the preparation of the samples.

APPENDIX: ABSOLUTE CALIBRATION USING PHONON SCATTERING

The measured intensity $I(\mathbf{Q}_0,\omega_0)$ at a particular position $\mathbf{Q}_0$ and ω_0 of the instrument is

$$I(\mathbf{Q}_0,\omega_0)=I_0\,\delta V\,\delta t\,n_v\exp[-2M(\mathbf{Q}_0)-2L(\mathbf{Q}_0)] \times\int S(\mathbf{Q},\omega)R(\mathbf{Q}-\mathbf{Q}_0,\omega-\omega_0)d^3\mathbf{Q}d\omega\ , \quad \text{(A1)}$$

with I_0, the incident intensity; δV, the effective sample volume; δt, the measuring time; n_v, the atoms/volume; $R(\mathbf{Q}-\mathbf{Q}_0,\omega-\omega_0)$, the instrumental resolution function;[40] and $S(\mathbf{Q},\omega)$, the scattering function. The integrated intensity of a constant-$\mathbf{Q}$ scan including the normalization factor[41] $N(\omega_0)$ gives the useful relation

$$I(\mathbf{Q}_0)=\int\frac{I(\mathbf{Q}_0,\omega_0)}{N(\omega_0)}d\omega_0 =I_0\,\delta V\,\delta t\,n_v\exp[-2M(\mathbf{Q}_0)-2L(\mathbf{Q}_0)] \times\int S(\mathbf{Q},\omega)d\omega\ , \quad \text{(A2)}$$

where $N(\omega_0)=\int\int R(\mathbf{Q}-\mathbf{Q}_0,\omega-\omega_0)d^3\mathbf{Q}\,d\omega$ is independent of $\mathbf{Q}_0$. For the coherent quasielastic scattering, the scattering function is $S_{\rm dif}(\mathbf{Q},\omega)$, as discussed above, and for one-phonon scattering at (ω_j), it is[42]

$$S_{{\rm ph},j}(\mathbf{Q},\omega)=|G_j(\mathbf{Q})|^2F_j(\omega,\omega_j,T)\ , \quad \text{(A3a)}$$

with

$$G_j(\mathbf{Q})=b(\hbar/2M)^{1/2}\sum_s(\mathbf{Q}\cdot\mathbf{e}_s^j)\exp(i\mathbf{Q}\cdot\mathbf{R}_s) \quad \text{(A3b)}$$

$$F(\omega,\omega_j,T)=[n(\omega)+1]\frac{\delta(\omega-\omega_j)}{\omega} \quad \text{(A3c)}$$

(when observed in neutron energy-loss spectroscopy), and M, the mass of the primitive unit cell; $\mathbf{e}_s^j$, the eigenvector of atoms at $\mathbf{R}_s$ in branch j; $n(\omega)$, the Bose-Einstein occupation number; and $\sum_s$, the sum over all atoms in unit cell. Note that the inelastic scattering is also affected by the static DWF arising from any disorder in the crystal. The existence of disorder-induced phonon scattering attenuation has been shown experimentally by Dosch *et al.*[42] Since the crystal structure and, subsequently, the structure factor of the host lattice phonons is known, the scattering intensity from any host lattice phonon can be used to calibrate the defect-induced scattering intensity into an absolute scale.

In principle $N(\omega_0)$ has to be calibrated for every position ω_0 along the constant-$\mathbf{Q}$ scan, but if the scattering function is much narrower in ω than the instrumental resolution, as is the case here, then $I(\mathbf{Q}_0)$ can be derived in a very good approximation by taking a peak height times peak width divided by $N(\omega_{\rm peak})$. In this way $I_{\rm dif}(\mathbf{Q}_0)$ has been determined from quasielastic scattering around $\omega=0$ at $\mathbf{Q}_0$ and $I_{{\rm ph},j}(\mathbf{Q}')$ from inelastic scattering around ω_j at $\mathbf{Q}'$. From this and Eq. (A3) it follows for the ratio $r_{\rm meas}=I_{\rm dif}(\mathbf{Q}_0)/I_{{\rm ph},j}(\mathbf{Q}')$

$$r_{\rm meas}=\frac{\exp[-2M(\mathbf{Q}_0)-2L(\mathbf{Q}_0)]}{\exp[-2M(\mathbf{Q}')-2L(\mathbf{Q}')]} \times\frac{S_{\rm dif}(\mathbf{Q}_0)}{|G_j(\mathbf{Q}')|^2[n(\omega_j)+1]1/\omega_j}\ , \quad \text{(A4)}$$

which is the general equation for the absolute calibration

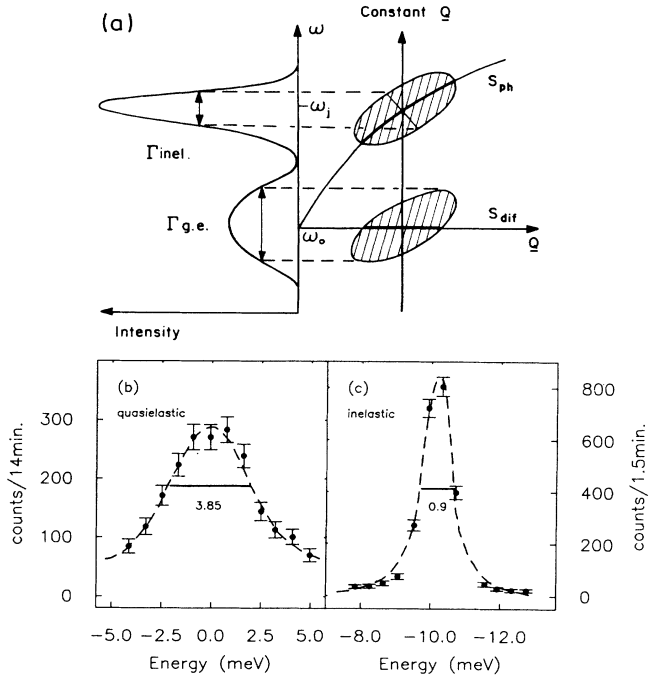

FIG. 10. Constant-$\mathbf{Q}$ scans for the absolute calibration: (a) schematic illustration in $\mathbf{Q}$-ω space; (b) constant-$\mathbf{Q}$ scan over the quasielastic line at $\mathbf{Q}=(3.6,0.6,0.6)$; (c) constant-$\mathbf{Q}$ scan over TA phonon at $\mathbf{q}=(0,-0.25,-0.25)$ in the (400) Brillouin zone. The results (b) and (c) are obtained in $NbD_{0.017}$. Note that the observed halfwidths are determined by the instrumental resolution.

TABLE II. Transverse-acoustic phonon intensities used for intensity calibration. For asterisk and I_{20} see text.

		BZ (200)		BZ (400)	
q $(2\pi/a)$	E (meV)	I_{exp}	I_{20}	I_{exp}	I_{20}
$(0,-0.2,-0.2)$	7.6	118.3	117.2	387.5*	358.5
$(0,-0.25,-0.25)$	10.2	63.9	68.7	293.5*	210.2
$(0,-0.3,-0.3)$	13.1	44.3	44.2	129.5	125.0

of $S_{dif}(\mathbf{Q}_0)$ by the measured integrated intensity ratio r_{meas}. In the case of NbD_x one can show that the static DWF $2L$ can be neglected in the discussed regime of the scattering vector and the defect concentration, thus, the relation (A4) is applicable by setting $2L(\mathbf{Q})=0$. In general (for higher defect concentrations and for heavily distorting defects), however, the static DWF cannot be ignored in the calibration equation (A4), but by measuring both scattering laws at the same $\mathbf{Q}$ value (say $\mathbf{Q}^*$), Eq. (A4) becomes independent of any Debye-Waller factor. (Note that $2M$ and $2L$ are only functions of the scattering vector $\mathbf{Q}$ and not of the energy transfer.[42]) In this special case, Eq. (A4) takes the simple form

$$S_{dif}(\mathbf{Q}^*)=r_{meas}\,|\,G_j(\mathbf{Q}^*)\,|^2[n(\omega_j)+1]\frac{1}{\omega_j}\ . \qquad \text{(A5)}$$

Since the instrumental resolution function $R(\mathbf{Q}-\mathbf{Q}_0,\omega-\omega_0)$ has been adjusted to the quasielastic measurement, it may often not be ideally suited to the inelastic calibration measurements. If the energy window of the instrument is wide (as it was in this study), this causes mainly two problems.

(i) The phonon peak may be broad and not well defined.

(ii) The low-energy tail of some phonons may be affected by strong quasielastic scattering and, thus, gives wrong integrated intensities.

Problem (i) can usually be solved by choosing those phonon excitations which can be measured in the so-called "focusing" geometry, where the long axis of the resolution ellipsoid in $\mathbf{Q}-\omega$ space is as parallel as possible to the slope of the inelastic scattering law [Fig. 10(a)]. By way of example we show in Figs. 10(b) and 10(c) the constant-$\mathbf{Q}$ scans of the quasielastic and the inelastic scattering law in the $NbD_{0.017}$ system.

Problem (ii) demands a careful data analysis, if an accurate absolute calibration is required. In this work we have employed a "self-consistency test" of the measured inelastic intensities which allows the elimination of even small, unwanted quasielastic scattering contributions. Three transverse-acoustic phonons have been measured in the two Brillouin zone (200) and (400). The observed integrated intensities I_{exp} (obtained by a Gaussian fit to the raw data) are shown in Table II. The intensity ratios of each two-phonon intensities $I_{ph,j}(\mathbf{Q}_i)$ and $I_{ph,l}(\mathbf{Q}_k)$ are, according to Eq. (A3), related by

$$\beta_{ijkl}=\frac{\omega_l}{\omega_j}\frac{n(\omega_j)+1}{n(\omega_l)+1}(\mathbf{Q}_i/\mathbf{Q}_k)^2\exp[2M(\mathbf{Q}_k)-2M(\mathbf{Q}_i)] \qquad \text{(A6)}$$

(The static DWF has been neglected for reasons given above.) Equation (A6) can be used for a simple algorithm which renders the measured phonon intensities iteratively self-consistent. The final intensities (I_{20} in Table II), obtained after 20 iterations, all have the same quality and can equivalently be used in Eq. (A4). By this analysis, quasielastic intensity contaminations are detected in the phonon intensities marked with *,[44] and, as a by-product, the error bar of the calibration measurement (3% in our case) is provided.

[1]See, e.g., *Hydrogen in Metals I*, Vol. 28 of *Topics in Applied Physics*, edited by G. Alefeld and J. Voelkl (Springer, Berlin, 1978).

[2]H. Dosch and J. Peisl, Phys. Rev. Lett. **56**, 1385 (1986).

[3]H. D. Carstanjen and R. Sizmann, Phys. Lett. **40**, 93 (1972).

[4]V. A. Somenkov, A. V. Gurskaya, H. G. Zemlyanov, M. E. Kost, N. A. Chernoplekov, and A. A. Chertov, Fiz. Tverd. Tela (Leningrad) **10**, 1355 (1968) [Sov. Phys.—Solid State **10**, 1076 (1968)].

[5]E. Burkel, H. Dosch, and J. Peisl, Z. Phys. B **53**, 33 (1983).

[6]S. A. Steward, Solid State Commun. **17**, 75 (1975).

[7]H. Behr, E. Burkel, H. Dosch, and J. Peisl (unpublished results).

[8]E. Burkel, H. Metzger, H. Behr, and J. Peisl, Phys. Rev. Lett. **46**, 1078 (1981).

[9]H. K. Birnbaum and C. P. Flynn, Phys. Rev. Lett. **37**, 25 (1976).

[10]T. Springer, in *Springer Tracts in Modern Physics*, edited by G. Höhler and E. Niekisch (Springer, Berlin, 1972), Vol. 40.

[11]K. W. Kehr, in *Hydrogen in Metals*, Ref. 1.

[12]V. Lottner, J. W. Haus, A. Heim, and K. W. Kehr, J. Phys. Chem. Solids **40**, 557 (1979).

[13]C. T. Chudley and R. J. Elliot, Proc. Phys. Soc., London **77**, 353 (1961).

[14]W. Gissler, G. Alefeld, and T. Springer, J. Phys. Chem. Solids **31**, 2361 (1970).

[15]H. Buchholz, J. Voelkl, and G. Alefeld, Phys. Rev. Lett. **30**, 318 (1973).

[16]G. C. Abell, Phys. Rev. B **20**, 4773 (1979).

[17]H. Sugimoto and Y. Fukai, Phys. Rev. B **22**, 670 (1980).

[18]H. Metzger, J. Peisl, and J. Wanagel, J. Phys. F **6**, 2195 (1976); see also H. Peisl, in *Hydrogen in Metals*, Ref. 1.

[19]G. S. Bauer, W. Schmatz, and W. Just, *Proceedings of the Second International Congress on Hydrogen in Metals, Paris, 1977* (Pergamon, New York, 1977).
[20]H. Dosch, diploma thesis, University of Munich, 1981; H. Dosch and J. Peisl (unpublished).
[21]H. Metzger, H. Behr, G. Steyrer, and J. Peisl, Phys. Rev. Lett. **50**, 843 (1983).
[22]M. A. Krivoglaz, *Theory of X-ray and Thermal Neutron Scattering by Real Crystals* (Plenum, New York, 1969).
[23]H. Trinkaus, Phys. Status Solidi B **51**, 307 (1972).
[24]P. H. Dederichs, J. Phys. F **3**, 471 (1973).
[25]G. E. Bacon, *Neutron Diffraction* (Clarendon, Oxford, 1975).
[26]E. Eisenriegler, Cryst. Lattice Defects **2**, 181 (1971).
[27]H. Kanzaki, J. Phys. Chem. Solids **2**, 107 (1957).
[28]For an introduction to elementary properties of the Kanzaki forces, see H. Wagner, in *Hydrogen in Metals,* Ref. 1.
[29]R. I. Sharp, J. Phys. C **2**, 421 (1969); V. Tewary, J. Phys. F **3**, 1515 (1973).
[30]H. G. Haubold and W. Schilling kindly made the basic program structures available to us.
[31]H. Pfeiffer and J. Peisl, Phys. Lett. **60A**, 363 (1977).
[32]V. Lottner and H. R. Schober, Phys. Rev. Lett. **42**, 1162 (1979).
[33]We define χ^2 as the mean-square deviation $(1/N)\sum_i [y_i - y(x_i)]^2$, where y_i are the experimental values, $y(x_i)$ the calculated values, and N the number of points.
[34]R. M. Cotts, in *Hydrogen in Metals,* Ref. 1.
[35]J. Vitko, Ph.D. thesis, Cornell University, 1976.
[36]D. Emin, Phys. Rev. Lett. **25**, 1751 (1970); Phys. Rev. B **3**, 1321 (1971).
[37]H. Wagner and H. Horner, Adv. Phys. **23**, 587 (1974).
[38]A. I. Shirley, C. K. Hall, and N. J. Prince, Acta Metall. **31**, 985 (1983).
[39]A. Magerl, J. J. Rush, J. M. Rowe, D. Richter, and H. Wipf, Phys. Rev. B **27**, 927 (1983).
[40]M. J. Cooper and R. Nathans, Acta Crystallogr. **23**, 357 (1967).
[41]B. Dorner, in *Coherent Inelastic Neutron Scattering in Lattice Dynamics,* Vol. 93 of *Springer Tracts in Modern Physics,* edited by G. Höhler and E. Niekisch (Springer, Berlin, 1982).
[42]H. Dosch, J. Peisl, and B. Dorner, Z. Phys. B **63**, 479 (1986).
[43]B. Dorner, Acta Crystallogr. A **28**, 319 (1972).
[44]Note that falsified inelastic scattering intensities are found for the low energetic phonons in the higher-order Brillouin zone, where the quasielastic scattering is strongest.